

A 3D LIF system for turbulent buoyant jet flows

Xiaodong Tian, Philip J.W. Roberts

636

Abstract A Laser-Induced Fluorescence (LIF) system for mapping the three dimensional tracer concentration field in turbulent flows is described. The system is particularly suited to studies of single or multiple buoyant jets discharged into unstratified and stratified flowing environments for conditions typical of wastewater discharges into surface water bodies. A laser beam is scanned through the flow and LIF images are obtained in parallel planes with a high-speed synchronized CCD camera. Refractive index matching is used to minimize refractive index variations due to local density gradients. An application to vertical round buoyant jets discharging into unstratified and stratified cross flows is presented. The three-dimensional system can obtain vastly more data than is possible with probe-based techniques and can yield far more insight into the flow and mixing processes.

Abbreviations

a	Combined attenuation coefficient, cm^{-1}
a_w	Attenuation coefficient for fresh water, cm^{-1}
B	Buoyancy flux of buoyant jet, cm^4/s^3
c	Tracer concentration, g/l
$C_{\text{salt}}, C_{\text{eth}}$	Salt and ethanol concentrations, g/l
d	Port diameter, cm
g	Acceleration due to gravity, cm/s^2
g'_0	Modified acceleration due to gravity at source, cm/s^2
Q	Volume flux of buoyant jet, cm^3/s
I	Image gray scale level, DN
l_a, l_Q, l_M, l_s, l_t	Buoyant jet length scales, cm (Eq. 8)
L_y	Distance from camera to image plane, cm
M	Momentum flux of buoyant jet, cm^4/s^2
M_y	Image scale factor

N	Buoyancy frequency, s^{-1}
u_a	Ambient flow velocity, cm/s
u_j	Jet exit velocity, cm/s
P	Laser power, W
S_0	Lowest dilution on the vertical center-plane through the nozzle
S_m	Minimum dilution: lowest dilution in a vertical plane perpendicular to the flow
x, y, z	Coordinates, cm
z_m	Maximum rise height of buoyant jets, cm
z_e	Equilibrium rise height of buoyant jets, cm
α	Image calibration constant
ρ_0	Effluent density, g/cm^3
ρ_a	Ambient density, g/cm^3

1 Introduction

Wastewaters and atmospheric pollutants are often released into the environment as turbulent buoyant jets, in order to generate efficient mixing and rapid dilution that substantially reduces the concentrations of potential pollutants. Although such flows have been extensively studied over many years, and many mathematical models of their behavior exist, laboratory experimental studies are still needed because of the complex nature of these flows, that may include merging of multiple jets, and the effects of boundaries, ambient flows, and density stratification.

The main objective of these experiments is usually to measure dilution. This has traditionally been done by adding a scalar tracer whose concentrations are measured with point-based techniques, either by in-situ probes or by the extraction of samples by suction from various points in the flow field. Examples of studies in water using a salt tracer with conductivity probes include Roberts (1979), Daviero (1998), Roberts et al. (2001), and with sample extraction include Wright (1977, 1984), and Roberts and Snyder (1993). These point-based techniques have some major deficiencies. The flow may be disturbed by the probes, the number of measurement points is very limited, and extraction techniques can yield only time-averaged concentrations and cannot capture their instantaneous fluctuations. The largest number of simultaneous samples obtained by a point-based technique may be Roberts and Snyder (1993), who used 100 sampling probes. Even this number causes severe spatial under-sampling, particularly for complex three-dimensional flows.

Received: 25 June 2003 / Accepted: 1 September 2003
 Published online: 22 October 2003
 © Springer-Verlag 2003

X. Tian, P.J.W. Roberts (✉)
 School of Civil and Environmental Engineering,
 Georgia Institute of Technology,
 Atlanta, GA 30332, USA
 E-mail: proberts@ce.gatech.edu

The writers acknowledge the support of the National Science Foundation under Grant Numbers. DGE-9354986 and CBT-8915537, and the STAR program of the U.S. Environmental Protection Agency, Exploratory Research, Physics, Grant Number R 826216. The authors express their gratitude to Dr. Walter Frick, U.S. EPA for his assistance.

The advent of Laser-Induced Fluorescence (LIF) techniques in the 1970s enabled simultaneous capture of the entire instantaneous tracer concentration field over a planar sampling area. LIF is a non-intrusive technique that is particularly applicable to turbulent buoyant jet flows. Many studies have been reported since the earliest ones by Owen (1976), including Dimotakis et al. (1983), Papanicolaou and List (1988), Prasad and Sreenivasan (1990), Ferrier et al. (1993), and Webster et al. (2001). Most of these studies were two-dimensional planar LIF (PLIF), which is now a widely used and well-established technique. Even relatively simple buoyant jet flows, particularly in cross flows, are inherently three-dimensional, however, and planar systems cannot reveal this three-dimensionality.

To overcome these deficiencies, three-dimensional LIF (3DLIF) systems have begun to appear. In these systems a laser sheet is swept through the flow at high speed and images captured with a synchronized camera. A cylindrical lens is often used to expand the laser beam into a sheet that is swept through the flow by an oscillating mirror, a rotating drum, or a rotating scanner as shown in Fig. 1. The most common optical arrangement consists of an oscillating mirror driven by a galvanometer (Fig. 1a). This system cannot create parallel laser sheets, so, to simplify post-processing, the laser sheets are usually assumed to be parallel. This limits the dimensions of the experimental section to be typically less than 50 mm wide. Configurations of this type were used by Kychakoff et al. (1987), Winter et al. (1987), Prasad and Sreenivasan (1990), Yip et al. (1988), Goldstein and Smits (1994), Brücker (1995), Merkel et al. (1994, 1996), Maas et al. (1994), and Ruck and Pavlovski (2000).

In the rotating drum system (Fig. 1b) small mirrors are attached to a circular drum in a helical pattern at equal intervals around its circumference. The mirrors are mounted at 45° so that the laser beam, which is initially parallel to the drum axis, is reflected perpendicular to it. The drum rotates with a constant angular velocity and the beam hits the mirrors sequentially resulting in parallel laser sheets. This configuration was used by Guezennec et al. (1994), Delo and Smits (1997), and Brücker (1997). Rotating scanners consisting of polygon mirrors have also been used (Figure 1c). While it has been common to create the laser sheet in 2D systems with this method, few researchers have applied it to three-dimensional systems

because of the optical complexity. This configuration was used by Patrie et al. (1994), Island et al. (1996), and Deusch (1998); discussions of scanner designs can be found in Rockwell et al. (1993) and Deusch (1998).

A major deficiency of laser sheets generated with cylindrical optics is their spatial variation of intensity. It is approximately Gaussian and is much brighter in the center than at the edges. This non-uniformity considerably complicates the extraction of quantitative tracer information, and severely limits the overall dynamic range of the measurements. These problems can be overcome by the use of orthogonal scanning mirrors. Dahm et al. (1991, 1992) used low inertia galvanometer oscillating mirrors that swept a laser beam in a raster scan fashion through the desired measurement volume. The advantage of this configuration is that the intensity of laser sheets can be made laterally uniform; the sheets are not parallel to each other, however.

The systems discussed above have been limited to short duration experiments in small volumes because of limited image storage capacity and low camera sensitivity. For example, in Dahm et al. (1991), a flow volume of $30 \times 30 \times 1$ mm was investigated. Increasing the area illuminated decreases the laser intensity, necessitating either higher laser power or increased fluorescent dye concentrations. But increasing the dye concentration increases the laser attenuation and causes the relationship between emitted light intensity and dye concentration to become nonlinear. These obstacles have gradually been overcome by recent advances in instrumentation, especially in optoelectronics, low-light high-speed cameras, high-speed scanning mirrors, image capture and processing techniques, and fast mass storage devices. Whereas it may have been necessary a few years ago to use expensive dedicated high-speed video systems, it is now possible to develop better systems at much lower cost.

Experiments on buoyant jet flows typical of wastewater discharges require relatively large-scale stratified test facilities. The large scale is necessary to maintain jet Reynolds numbers high enough to ensure that they are turbulent. Stratification causes difficulties with LIF because the density variations produce refractive index variations that cause random fluctuations in laser intensity. This has limited most previous studies to situations with small density differences and/or a small region of

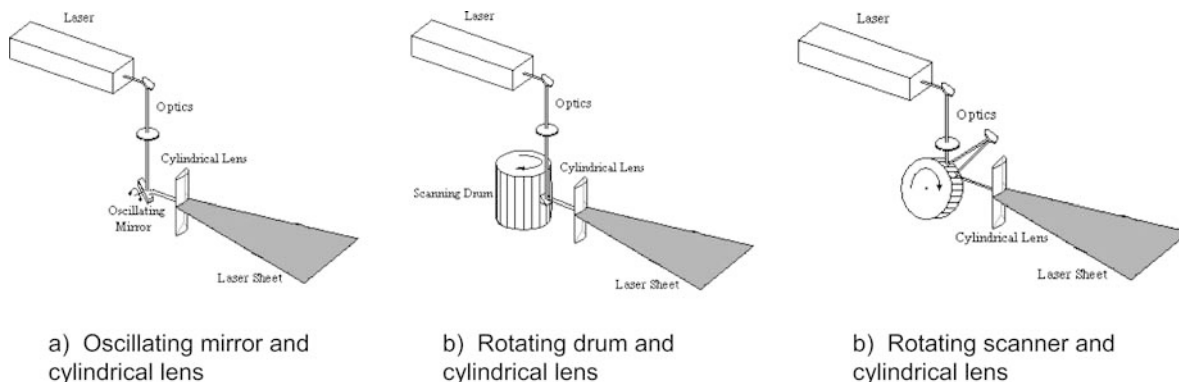


Fig. 1. Three types of scanning mirror systems

interest. These limitations can be overcome by refractive index matching in which liquids of different density but equal refractive index are used.

In this paper, a 3DLIF system that is capable of measuring three-dimensional concentration fields continuously and almost instantaneously in fairly large stratified test facilities is described. System validation and applications to a vertical round buoyant jet discharging into a homogeneous and linearly-stratified cross flow are discussed. For more details of the system and applications to other flows, see Tian (2002).

2 Experimental

A schematic depiction of the experimental configuration is shown in Fig. 2. The test facility is a tow tank 6.10 m long by 0.91 m wide by 0.61 m deep. The front wall consists of two three-meter long glass panels to enable long duration tows with unobstructed views; the left wall is also glass to allow optical access for the laser. The right and rear walls and floor are steel, coated with black epoxy paint to resist corrosion and to reduce reflections. The tank can be stratified using a two-tank filling system (Daviero et al. 2001). A towing carriage rides on two precision one-inch diameter stainless steel rails that run the length of the tank. The carriage is propelled via a chain and gear system by a 130 volt Bodine motor connected in series to a Penta-Drive DC motor speed control device. The effluent, usually a mixture of water, salt (NaCl), and fluorescent dye, is supplied from a reservoir by a rotary pump at a flowrate measured by a precision rotameter. The fluorescent dye is Rhodamine 6G, whose characteristics are given in Ferrier et al. (1993).

The beam from a continuous wave Argon-Ion laser strikes two orthogonal fast galvanometer scanning mirrors that move the beam in the horizontal (y) and vertical (z) directions. The beam then strikes a plano-convex lens of 250 mm diameter, 940 mm focal length. The scanning mirrors are located at the focal point of this lens, so that the beam is always refracted parallel to the axis of the tow

tank. The laser causes the dye to emit fluoresced light that is captured by a high speed CCD digital camera. The camera is attached to the tow carriage and moves with it so that the discharge appears to be stationary relative to the camera in a flowing environment.

The system employs two computers, one for overall timing control, and one for image acquisition. The timing control computer drives the laser beam and synchronizes it with image capture by means of a National Instruments Multifunction I/O Board (Model PCI-MIO-16E-4). This board is programmed in LabView to provide two analog voltage signals that control the motion of the scanning mirrors, and a TTL digital signal to trigger image acquisition. The analog signals are converted at a resolution of 12 bits from a digital file.

The CCD camera is a Dalsa CA-D6. This digital camera provides output in 8-bit resolution; in other words 256 gray scale levels. The resolution (number of active pixels) is 532 by 516. It uses a LVDS (Low Voltage Differential Signal, also known as EIA-644) data format that enables high data transmission rates over long cable lengths. The maximum frame rate of this camera is 260 frames per second, which gives a data rate of 71 MHz. This high rate is achieved by four taps, each capable of 25 MHz. The camera has a high-gain A/D converter to enable use with low light levels, but the noise level is still quite low (Tian 2002). For the experiments reported here a Fujinon CCTV camera lens of 25 mm focal length and $f0.85$ aperture was used. A long pass orange filter (Schott glass 530) with a sharp cutoff centered on 530 nm is placed between the camera lens and imaging chip to pass only the fluoresced light and to eliminate the laser scattered light.

The image acquisition and processing computer contains a Bitflow RoadRunner frame grabber board controlled by Video Savant software. The computer has four hard drives that are controlled by an Adaptec Ultra160 SCSI card. This allows streaming the images to the four discs simultaneously in real time at up to the maximum camera rate of 260 frames per second. The total capacity of the hard drives is 32.4 GB so we are not limited by storage

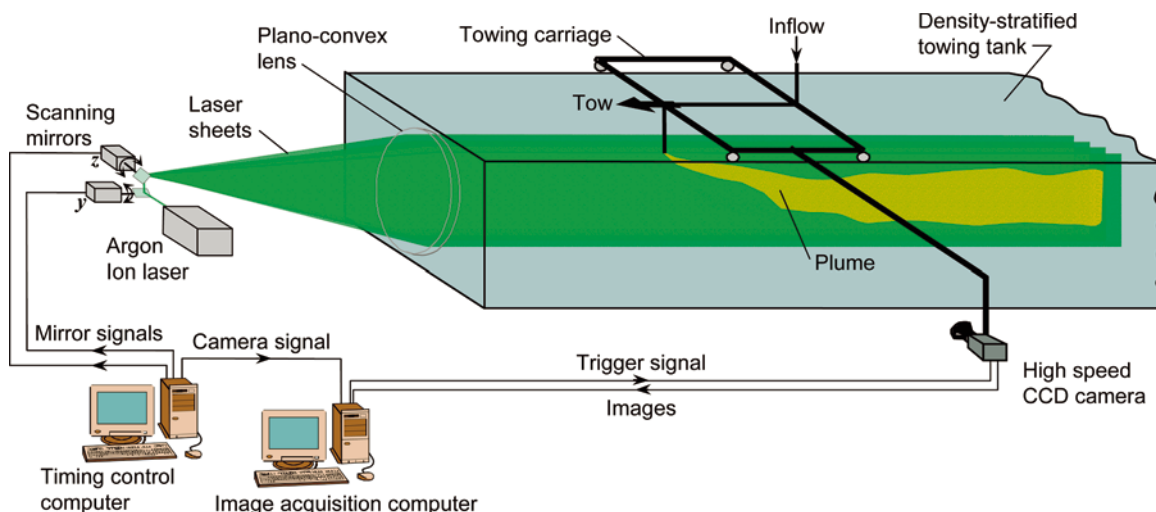


Fig. 2. Schematic depiction of 3DLIF system

in computer memory and can perform long duration experiments.

A schematic of the timing control is shown in Fig. 3. An experiment commences with the I/O board sending an analog voltage to move the vertical (z) mirror. Simultaneously, the board sends a TTL signal to the frame grabber board, which in turn sends an LVDS signal to the camera to begin image acquisition (exposure). The laser beam makes one sweep up and down while the camera is exposing (so the shutter is “open”). A voltage is then sent to the y mirror to move the beam a small distance horizontally and a TTL signal is sent to trigger download of the previous frame, clear the camera buffer, and begin the next exposure. There is a 0.1 ms delay between exposures to download the previous frame. This is repeated so that multiple vertical “slices” through the flow are obtained. After a predetermined number of slices, the beam returns to the starting point and the cycle starts again.

A major advantage of this system is that it affords great flexibility to easily vary parameters in order to optimize them for the particular flow under study. The laser sheet height, number of slices, their separation, and scanning frequencies are fully and easily controllable. In addition, all of the laser sheets are parallel, simplifying post-processing operations. For the experiments reported here, the effluent (source) dye concentration was 500 to 1500 $\mu\text{g/L}$, so that concentrations in the flow field are around 15 to 30 $\mu\text{g/L}$. The laser power is 2.0 W, the camera speed is 100 frames per second, the area imaged is $60 \times 20 \times 20$ cm, and the number of slices ranges from 20 to 40 spaced typically 4 to 7 mm apart. The image resolution is therefore about 1.0 mm. At 100 frames per second with 20 slices, five full 3D fields are taken per second, so that the effective sample rate is 5 Hz. About 5 million points are sampled every 0.2 s, clearly vastly greater than possible with point probe methods. The data acquisition rate is about 1.5 GB/minute.

The individual three dimensional visualizations are actually reconstructions of multiple planar images obtained sequentially through the flow. For this to be a good approximation of the instantaneous flow field, the spatial and temporal resolutions must be chosen appropriately. Ideally, fields would be obtained rapidly enough that they represent a “frozen” image of the flow. Typical jet velocities in these experiments are 0.05 to 1.2 m/s and cross flow velocities are 10 to 40 mm/s. Therefore, the 5 Hz

sampling rate is too slow to freeze the smallest turbulent scales (the Kolmogorov scales), although the larger scales are frozen. Note that for capture of time-average results, which is the main objective of this research, the speed of capture is irrelevant; it is only important in the capture and display of instantaneous fields.

3 Calibration and corrections

The camera is focused on the center plane but images obtained off this plane will have a different geometric scale and may be out of focus. Defocusing was tested by obtaining images of a test pattern at various distances without refocusing. The images remained in acceptable focus at least up to ± 19.0 cm from the center plane (Tian 2002). For the experiments here, the largest distances are ± 12.0 cm, so the defocusing problem can be ignored. The change in image magnification cannot be neglected, however. If the distance from the camera imaging chip to the central image plane is L_{y_0} , from simple geometry the scale factor M_y (cm/pixel) for an image plane at distance L_y is:

$$M_y = \frac{L_y}{L_{y_0}} M_{y_0} \quad (1)$$

where M_{y_0} is the scale factor for the central plane, which is obtained by taking an image of a reference grid prior to each experiment.

While flow visualization with 3DLIF is fairly easy, extraction of reliable quantitative scalar concentration data is quite difficult. For Rhodamine dye concentrations less than about 50 $\mu\text{g/L}$, the relationship between the concentration c and image gray scale level I (DN, Digital Number) is linear:

$$c = \alpha I \quad (2)$$

where α ($\mu\text{g/l/DN}$) is the coefficient of proportionality. This coefficient must be measured as it depends on many factors including local laser intensity, exposure time, area illuminated, and camera lens transmittance and sensitivity. It also varies with the distance of the image plane from the camera. This variation is caused by two main factors. First, the plano-convex lens does not refract the laser beam perfectly parallel to the tank axis. The height of the laser

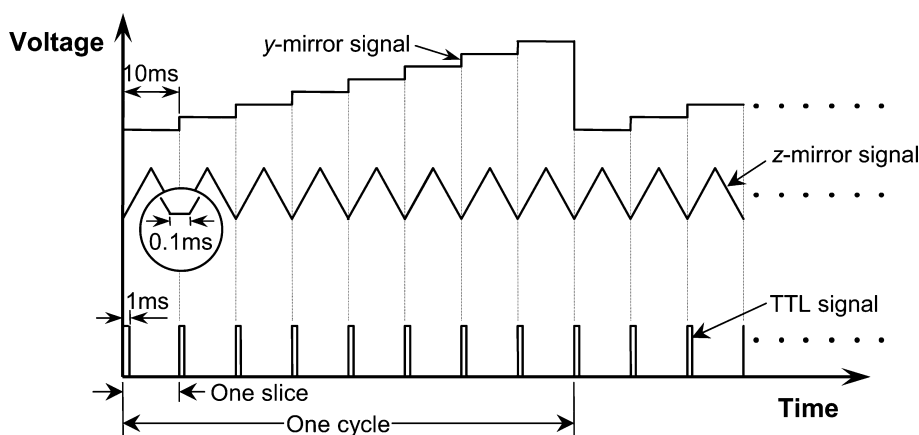


Fig. 3. Schematic of timing control (camera speed is 100 frames per second)

sheet varies, with the central sheet being tallest and those on each side smaller. Second, the path length of the fluoresced light as it travels through the water to the camera changes, resulting in varying attenuation. The values of α are obtained from images, taken prior to each experiment, of a Lucite tank 5.0 cm wide by 28.0 cm deep by 50.0 cm tall containing known dye concentrations. α typically varies by about $\pm 10\%$ over an image distance variation of ± 15 cm and individual values, α_j are used for each laser sheet.

Extensive post-processing is needed to extract quantitative concentration data from the raw data images. The gray scale levels of images of a white board illuminated by a uniform light source (a “standard” image) and a black-level image obtained by covering the lens are shown in Figures 4a, b. The images would be uniform for a perfect lens and sensor. The standard image is actually brighter at the center and darker at the edges, a phenomenon known as vignetting. The standard and blacklevel images also show four brighter bands about 10 pixels wide. These bands separate the four taps, each 133 by 516 pixels, that are required to achieve the very high data transmission rates. In the blacklevel image, intensities in the bands are around 10 DN and elsewhere around 5 DN. To correct for these variations, the blacklevel image is first subtracted from each raw image and from the standard image. The new raw images are then divided by the new standard image, pixel-by-pixel, to obtain the corrected pixel value $I_c(i, k)$:

$$I_c(i, k) = K \frac{I_r(i, k) - I_b(i, k)}{I_s(i, k) - I_b(i, k)} \quad (3)$$

where $I_r(i, k)$, $I_s(i, k)$, and $I_b(i, k)$ are the pixel values of the raw, standard, and blacklevel images respectively, (i, k) are the pixel indices, and K is the average pixel value in the standard image. The corrected image is shown in Fig. 4c.

Attenuation of the laser beam as it traverses the tow tank can be significant and must be accounted for. The rate of attenuation depends on the local concentrations of salt, ethanol, and fluorescent dye; ethanol, in particular, greatly increases the attenuation. Discussions of attenuation can be found in Koochesfahani and Dimotakis (1985),

Walker (1987), Van Cruyningen et al. (1990), Ferrier et al. (1993), and Daviero et al. (2001). The laser power decays exponentially with distance as:

$$P = P_0 e^{-a(x-x_0)} \quad (4)$$

where P is the power at location x , P_0 is the laser intensity at location x_0 , and a is the attenuation coefficient. The effects of the various solutes are additive, so the combined attenuation coefficient can be computed from (Daviero et al. 2001):

$$a = a_w + 0.000124C_{\text{salt}} + 0.000547C_{\text{eth}} + 0.00023c \quad (5)$$

where C_{salt} and C_{eth} are the concentrations of salt and ethanol in g/l, c is the Rhodamine concentration in $\mu\text{g/l}$, and a_w is the clear water attenuation coefficient. Even with filtering, the clear water attenuation coefficient a_w varied daily from about 0.0011 to 0.0045 cm^{-1} . It was therefore measured before each experiment by obtaining images of a Lucite cylinder containing a known dye concentration at two different locations in the tow tank.

Dye concentrations are computed from each raw image by the following procedure. The lens and sensor corrections are first applied to each raw image by Eq. 3. The value of α_j is then computed from the calibration images. This includes laser attenuation along the tow tank and so depends on the tow-carriage position. The dye concentration is then computed for the pixel at the top-left corner of each image by Eq. 2. The laser beam is assumed to be always parallel to the tow tank axis, so we proceed pixel-by-pixel for each horizontal line according to:

$$I_{cc}(i, k) = \frac{I_c(i, k)}{e^{-\sum_{m=1}^i (a_m \Delta x)}} \quad (6)$$

where I_{cc} is the adjusted pixel value, Δx the spacing in centimeters between two adjacent pixels, and a_m the local attenuation coefficient from Eq. 5. Finally, the dye concentration is computed from Eq. 2. Note that a_m is variable; it is calculated from the local concentrations of salt, ethanol, and fluorescent dye. This is done for all pixels in the image. The carriage position is then updated according to the known tow speed, new values of α_j are computed,

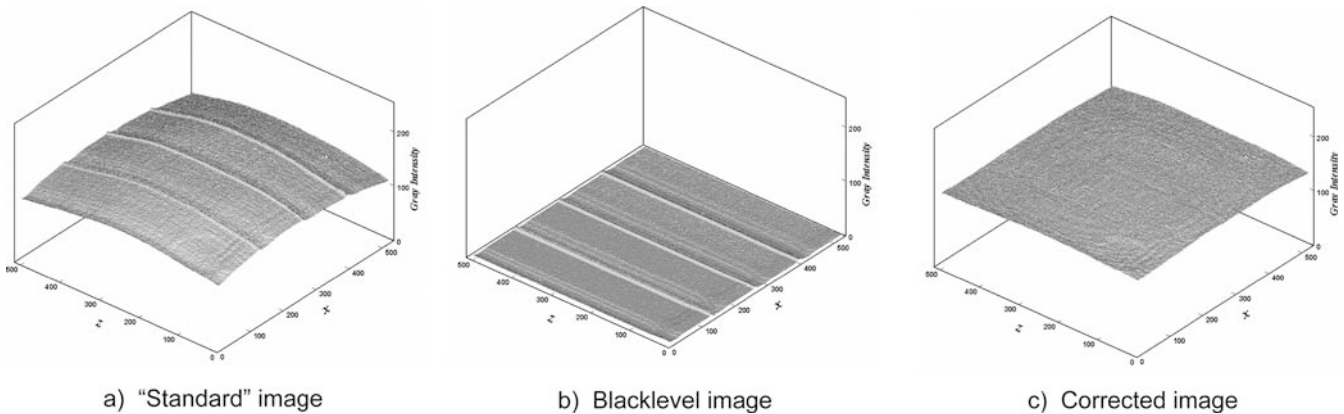


Fig. 4. Gray scales of images showing lens and sensor correction procedure

and the dye concentrations are computed for the next image. This is repeated for all images.

4

Experimental errors

Errors arise from measurement uncertainties and optical misalignments. The measurement errors include uncertainties in flowrate, tow speed, ambient and effluent densities, image magnification, and tracer concentration (including image capture, calibration, and corrections). Alignment errors include slight uncertainties in orientations of the mirrors, lenses, and the camera. Considerable efforts were made to minimize these errors in order to obtain reliable and repeatable results. Experiments on a homogeneous round jet in a stagnant uniform environment (next section) showed that the misalignment errors are negligible. The error of the precision rotameter is 3% (provided by the manufacturer). The tow speed was measured by timing the passage of the carriage between two points a known distance apart; its error is about 1%. The ambient and effluent densities were measured with an accuracy of ± 0.0001 g/cc. The image magnification was measured from images of regular grids; its error is 1%.

Uncertainties in tracer concentration are the main source of error. The image digitization error is estimated as 2%. This error decreases with increasing image brightness because the signal to noise ratio increases. The uncertainty in the calibration constant results from errors in the dye solutions and image capture; its error is about 4%. Additional errors introduced by the lens and attenuation corrections are estimated as 1% for unstratified environments and 4% for stratified environments. Combined, these result in a concentration measurement error of about 5% for unstratified environments and 7% for stratified environments. For experiments with multiport diffusers (discussed in other papers), further uncertainties include diffuser orientations (the diffuser should be perpendicular to the tank wall), port heights (all ports should be at the same level), and deviations of the false floor from horizontal (for unstratified experiments). The total discharge is assumed to be distributed uniformly to each individual riser; slight non-uniformity could contribute further errors. All of these uncertainties are small compared to the measurement error in concentration. The error for multiport diffuser experiments is estimated to be less than 8%.

5

System validation

The 3DLIF system and post-processing software was tested by applying it to a homogeneous round jet in a uniform stagnant fluid. This flow has been extensively studied and much data are available for comparison. The experimental parameters were: nozzle diameter, $d = 4.0$ mm; jet exit velocity, $u_j = 0.67$ m/s; source concentration, $c_0 = 350$ $\mu\text{g/L}$; camera speed = 100 frames per second; number of slices, $n_s = 40$; distance between slices, $\Delta z = 5.0$ mm; duration of recording = 60 s; and fresh water attenuation coefficient, $a_w = 0.0035$ cm^{-1} .

Reconstructed 3D images of the time-averaged tracer concentration field are shown in Fig. 5. In Fig. 5a, one

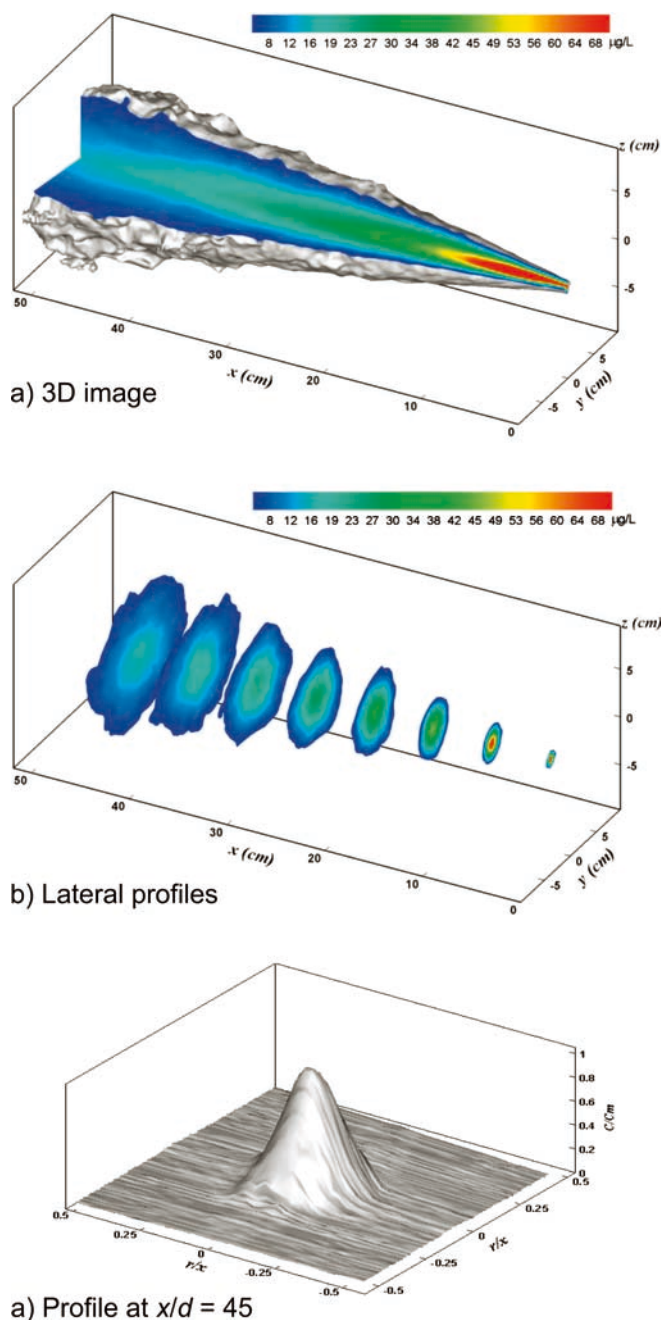


Fig. 5. Concentration distributions in a simple round jet

quarter of the jet is removed to show the inner concentration distribution with pseudo-color on two orthogonal longitudinal planes that intersect on the centerline. The outer jet surface is shown by extracting an iso-surface with a low threshold value. Fig. 5b shows lateral profiles at various distances from the nozzle, and Fig. 5c shows one profile in three-dimensional relief at a distance $x = 18$ cm ($x/d = 45$) from the nozzle. These visualizations successfully reconstruct the pure jet and clearly show the concentration distributions in three planes. The symmetry and the familiar Gaussian concentration distribution are apparent.

The decay of the mean concentration along the jet centerline is shown in Figure 6. It agrees closely with the semi-empirical equation (Fischer et al. 1979),

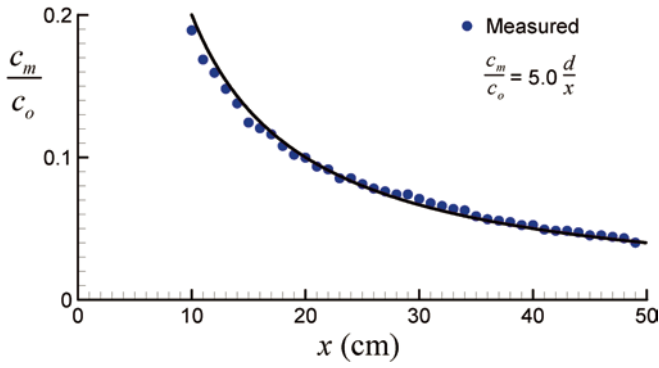


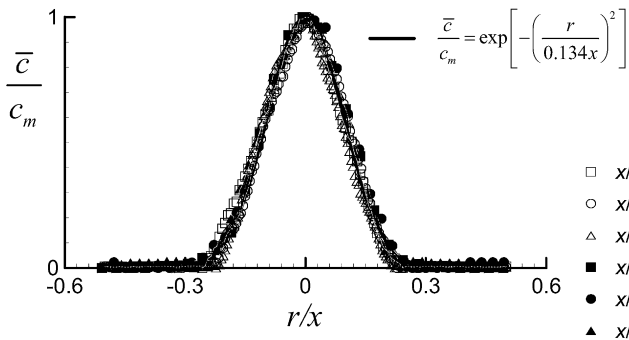
Fig. 6. Mean concentrations along the jet centerline

$c_m/c_o = 5 \cdot d/x$, where c_m is the centerline concentration. Profiles of mean concentration, \bar{c} , and the standard deviation of the concentration fluctuations, \tilde{c} , at various distances are shown in Fig. 7. Three of these were extracted from the vertical center plane (denoted by “V”), and three from the horizontal center plane (denoted by “H”). They were obtained far beyond $6d$ from the jet nozzle, so all profiles were in the Zone of Established Flow (ZEF). The profiles are symmetric about the centerline. The mean profiles agree closely with the Gaussian curve suggested by Fischer et al. (1979), $\frac{\bar{c}}{c_m} = \exp \left[-(r/b_c)^2 \right]$, where r is the radial distance from the centerline, and b_c is the half-width of the concentration field, estimated to be $0.134x$. The coefficient 0.134 is slightly higher than the average (0.127) of several experimental data sets reported by Fischer et al. (1979), but is within the range of quoted values ($0.101 < b_c < 0.156$). The standard deviation profiles are normalized by c_m . They are also symmetric about the centerline and collapse onto a self-similar shape. The peak is displaced from the centerline and its location is at approximately $r/x = 0.1$. These results agree closely with those obtained by Webster et al. (2001).

6 Applications

6.1 Introduction

Many investigations of various flows have now been conducted with the 3DLIF system. Here we give an example of



a) Mean concentration

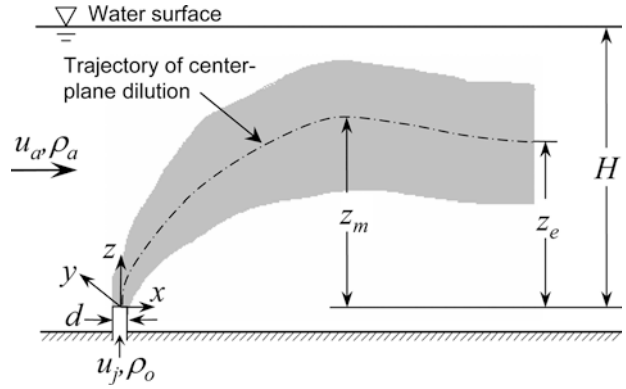


Fig. 8. Definition sketch for vertical buoyant jet in a cross flow

experiments on a round vertical buoyant jet discharging into unstratified and stratified crossflows. The experiments were conducted as shown in Fig. 2; a more dense effluent was discharged downwards near the water surface. This is a more convenient configuration than a positively buoyant jet discharged from the tank floor, particularly for towed experiments. This inverted modeling technique is permitted because variations in the fluid density throughout the flow field are small and are only important in the buoyancy forces (the Boussinesq assumption). The results are reported here as inverted (as a positively buoyant effluent discharging upwards).

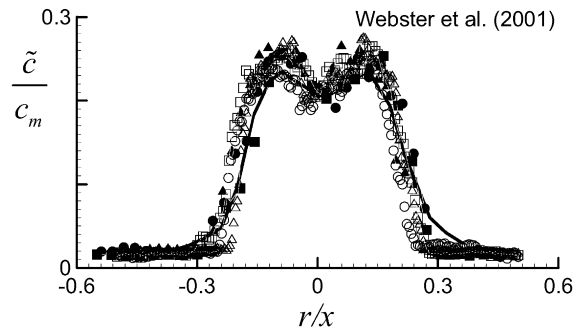
A definition sketch is shown in Fig. 8. The basic parameters are the port diameter, d , jet exit velocity, u_j , effluent density, ρ_o , ambient density, ρ_a , and ambient flow velocity u . Following Wright (1984), z_m is the maximum rise height (defined as the height to the level of maximum concentration at the maximum vertical dye penetration) and z_e is the equilibrium rise height (the rise height to the level of maximum concentration at the equilibrium spreading layer). An alternate set of parameters is:

$$\text{Volume flux, } Q = \frac{\pi}{4} u_j d^2 \quad (7a)$$

$$\text{Momentum flux, } M = u_j Q \quad (7b)$$

$$\text{Buoyancy flux, } B = g'_0 Q \quad (7c)$$

where $g'_0 = g \frac{\rho_a - \rho_o}{\rho_o}$ is the modified acceleration due to gravity, and g is the acceleration due to gravity. Following



b) Standard deviation of concentration fluctuations

Fig. 7. Self-similar mean profiles in a simple jet

Fischer et al. (1979), Wright (1984) and others, a set of length scales that relate to the flow behavior can be defined. The most important ones are:

$$l_Q = \frac{Q}{\sqrt{M}}, l_M = \frac{M^{3/4}}{\sqrt{B}}, l_t = \frac{\sqrt{M}}{u}, l_s = \frac{B}{u^3}, l_a = \frac{u}{N} \quad (8)$$

where $N = \sqrt{-\frac{g}{\rho_0} \frac{d\rho}{dz}}$ is the buoyancy frequency.

Conditions for the two experiments are summarized in Table 1. Except for stratification, the parameters for the two experiments are essentially the same. For the stratified experiment the ambient density profile was linear, and refractive index matching (Daviero et al. 2001) was used.

6.2

Results

Wright (1977) defines the flow as being in the momentum dominated far field (MDFF) when $z \gg l_t$ and in the buoyancy dominated far field (BDFF) when $z \gg l_s$. The effect of jet nozzle geometry is negligible if $z \gg l_Q$, and the flow behavior is controlled by buoyancy when $z \gg l_M$. In the experiments here, the camera saturated near to the nozzle so no quantitative data were obtained there. The discussions are focused on the region where $z \gg l_M$ (therefore, $z \gg l_Q$ and $z \gg l_s$), in other words, the effect of jet geometry is negligible and the flow is expected to be in the BDFF. The BDFF is also sometimes referred to as an advected thermal.

Figures 9a, b, c, d show instantaneous and time-averaged views of the outer jet surface and internal concentration distribution. The outer surfaces were obtained by computing and plotting an iso-surface of a concentration value set just above a minimal threshold value. These surfaces are made semi-transparent to show the variations of tracer concentration in the vertical plane through the jet centerline in pseudo-color. Animated movies have also been made to show the temporal variations of the instantaneous outer surface and center plane concentrations. For the unstratified experiment, the jet rises

indefinitely. For the stratified case, it reaches a terminal rise height and then spreads laterally; it is flatter than in the unstratified flow due to suppression of vertical motions by the stratification.

Concentration distributions in any plane can be obtained by computer graphics techniques. Lateral cross sections at various downstream locations are shown in Figures 9e, f. These show the familiar kidney shapes with the maximum concentrations occurring on each side of the center plane. The kidney shape for the stratified environment is initially similar to that of the unstratified flow, but it becomes less pronounced further downstream as it is compressed vertically by the ambient stratification.

The center-plane dilution S_0 (defined as the lowest value of dilution in the vertical plane through the nozzle center parallel to the flow direction) for the unstratified experiment is shown in normalized form in Fig. 10. The results are compared with the semi-empirical relation obtained by Wright (1984) for the BDFF:

$$\frac{S_0 Q}{u l_s^2} = 0.25 \left(\frac{z}{l_s} \right)^2 \quad (9)$$

A better fit to the data is:

$$\frac{S_0 Q}{u l_s^2} = 0.28 \left(\frac{z}{l_s} \right)^2 \quad (10)$$

which is close to Wright's result.

The minimum dilution, S_m (the lowest value of dilution in a vertical plane perpendicular to the flow) occurs to each side of the central plane. Dilutions and their trajectories are plotted in Figures 11a, b versus downstream distance, x , rather than height, z , because S_m and S_0 occur at different heights in the same cross section. The center-plane dilution trajectories (see Fig. 8) were extracted from the images by drawing a smooth curve halfway between the upper and lower jet boundaries, similar to the procedure of Wright (1984). This trajectory is very close to that of the lowest dilution in the center plane. The results are compared with the semi-empirical relation obtained by Wright (1984) for the BDFF:

$$\frac{z}{l_s} = 1.7 \left(\frac{x}{l_s} \right)^{2/3} \quad (11)$$

A better fit to the data is:

$$\frac{z}{l_s} = 1.64 \left(\frac{x}{l_s} \right)^{2/3} \quad (12)$$

which is again close to Wright's result. Substitution of Eq. 10 into Eq. 12 yields:

$$\frac{S_0 Q}{u l_s^2} = 0.75 \left(\frac{x}{l_s} \right)^{4/3} \quad (13)$$

which agrees well with the experimental results. The minimum dilution results were fitted with the empirical curve:

$$\frac{S_m Q}{u l_s^2} = 1.67 \left(\frac{x}{l_s} \right) \quad (14)$$

Table 1. Summary of the vertical buoyant jet experiments

Parameter	Unstratified	Stratified
Nozzle diameter, d	4.0 mm	4.0 mm
Effluent flowrate, Q	3.14 cm ³ /s	3.14 cm ³ /s
Source concentration, C_0	800 µg/L	600 µg/L
Camera speed	100 fps	100 fps
Number of slices, n_s	20	20
Distance between slices, Δz	8.7 mm	8.7 mm
Attenuation coefficient in fresh water, a_w	0.0011 cm ⁻¹	0.0020 cm ⁻¹
Duration of recording	35 s	35 s
Cross flow velocity, u	40 mm/s	40 mm/s
Density difference at nozzle level, $\Delta \rho_0$	0.0280 g/cm ³	0.0260 g/cm ³
Reynolds number, Re	1004	1004
Momentum flux, M	78.5 cm ⁴ /s ²	78.5 cm ⁴ /s ²
Buoyancy flux, B	86.2 cm ⁴ /s ³	80.0 cm ⁴ /s ³
Buoyancy frequency, N	–	0.38 s ⁻¹
l_Q	0.35 cm	0.35 cm
l_M	2.84 cm	2.96 cm
l_t	2.22 cm	2.22 cm
l_s	1.35 cm	1.26 cm
l_a	–	10.5 cm

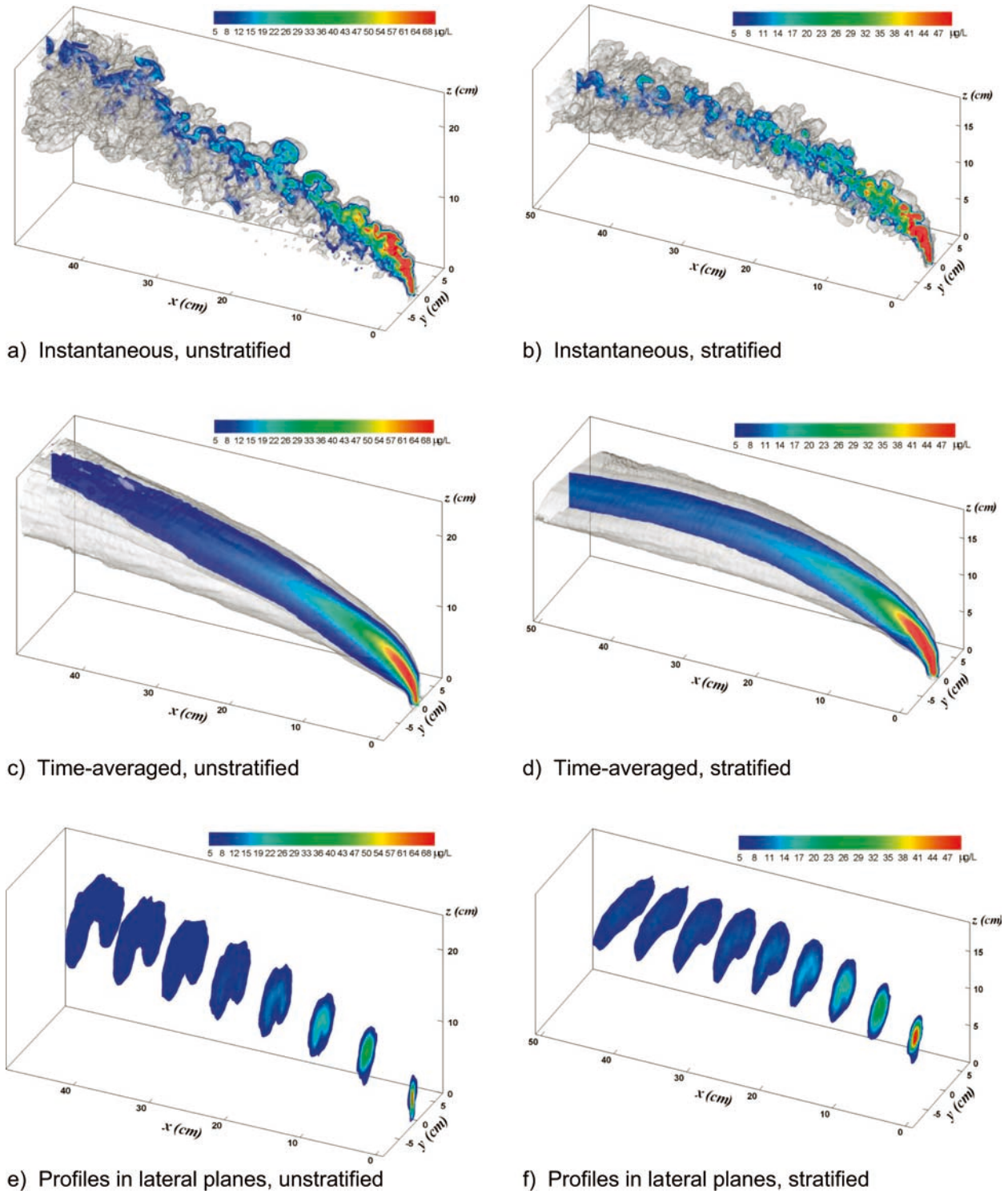


Fig. 9. Tracer concentrations of vertical buoyant jets in unstratified and stratified crossflows

which has a different power law relation than for center-plane dilution. The minimum and center-plane dilutions are initially very close. They diverge downstream as the kidney shape develops, and the ratio S_m/S_0 decreases from 1.0 to 0.72 in the range of $10 \leq x/l_s \leq 33$. This contradicts the result of Chu (1979), who suggested a constant ratio, $S_m/S_0 = 0.6$, based on two measurements. He did not give the locations of where these measurements were obtained so no further comparison can be made.

Not only can the variation of minimum dilution be obtained with the 3DLIF system, its trajectory can be easily extracted. As this trajectory is three-dimensional and diverges from both sides of the central plane, it would be very difficult to obtain either from traditional point measurement techniques or by PLIF. The trajectories of minimum and center-plane dilutions are shown in Fig. 11b. The best fit to the minimum dilution trajectory is:

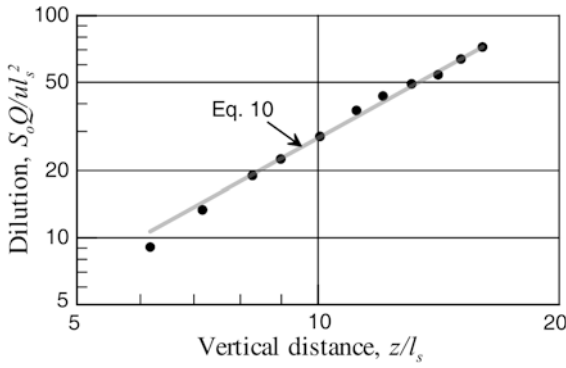


Fig. 10. Center-plane dilution of vertical buoyant

$$\frac{z}{l_s} = 3.6 \left(\frac{x}{l_s} \right)^{1/3} \quad (15)$$

which is much flatter ($z \sim x^{1/3}$) than the center-plane dilution trajectory ($z \sim x^{2/3}$).

The corresponding results for the stratified experiment, and comparisons with the unstratified equations, are shown in Figures 12a, b. The maximum rise height, $z_m = 13.8$ cm, is very close to the value of 13.4 cm obtained from the empirical relation suggested by Wright (1984):

$$\frac{z_m}{l_s} = 2.3 \left(\frac{l_a}{l_s} \right)^{2/3} \quad (16)$$

The stratification has little effect on dilutions or trajectories close to the source, and Eqs. 12, 13, and 14 can be used. Stratification begins to affect the jet farther downstream, at $x/l_s > 15$, and for $x/l_s > 25$, both the rise height and dilution become constant as the jet levels off. The minimum dilution again occurs off the center plane. Close to the nozzle ($x/l_s < 15$), the minimum and centerline dilutions are similar and are close to the unstratified values. Further downstream, the ratio S_m/S_0 continually decreases for the unstratified case (from 1.0 to 0.72 in the range of $10 < x/l_s < 33$), whereas in the stratified case the ratio becomes constant, equal to 0.95 for $x/l_s > 25$.

6.3

Other experiments

In addition to the experiments described here, the 3DLIF system has been applied to a wide range of wastewater outfall discharges. These include mixing of water produced from offshore oil production (Roberts and Tian 2002a), mixing of a thermal discharge (Roberts and Tian 2002b), to sewage discharged from the Boston tunneled outfall (which has multiport risers, Roberts et al. 2002), and to a proposed nickel mine outfall (Roberts and Tian 2003).

7

Conclusions

A 3DLIF system particularly suited to experiments on buoyant jet flows typical of wastewater discharges in stratified flows is described. Previous systems have been limited to short duration experiments in small volumes due to limited image storage capacity and low camera sensitivity. In the new system, two high-speed oscillating mirrors are used to create parallel laser sheets of uniform intensity that scan through the flow. A synchronized high-sensitivity camera captures images with low dye tracer concentrations. The images are written to multiple hard discs in real time, which allows an essentially unlimited recording time. The system is combined with refractive index matching to enable its use in fairly large-scale facilities in stratified environments. The system is fast enough to “freeze” the largest turbulent scales, but not the smallest ones. A faster, more sensitive camera would be necessary for this.

An application to a vertical round buoyant jet discharging into unstratified and stratified cross flows is reported. Three-dimensional visualizations were reconstructed that clearly show the spatial concentration distributions. These are the first known of such images obtained experimentally. Quantitative results include the spatial variations of minimum and center-plane dilutions and their trajectories. The center-plane results agree closely with previous relations suggested by Wright (1984). The stratification had no effect close to the source, but it reduced the rise height and dilution further downstream and caused a flattening of the plume near its terminal rise height.

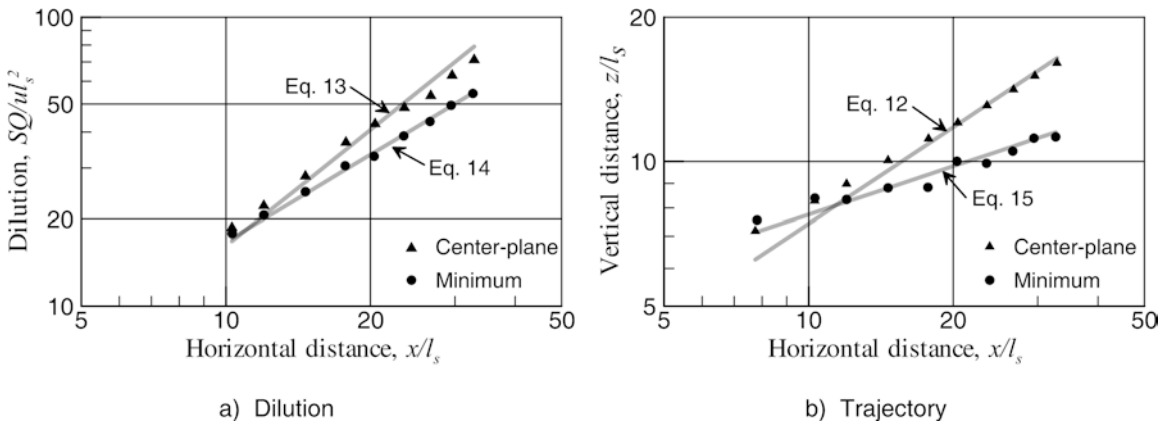


Fig. 11. Center-plane and minimum dilutions and their trajectories for unstratified cross flow

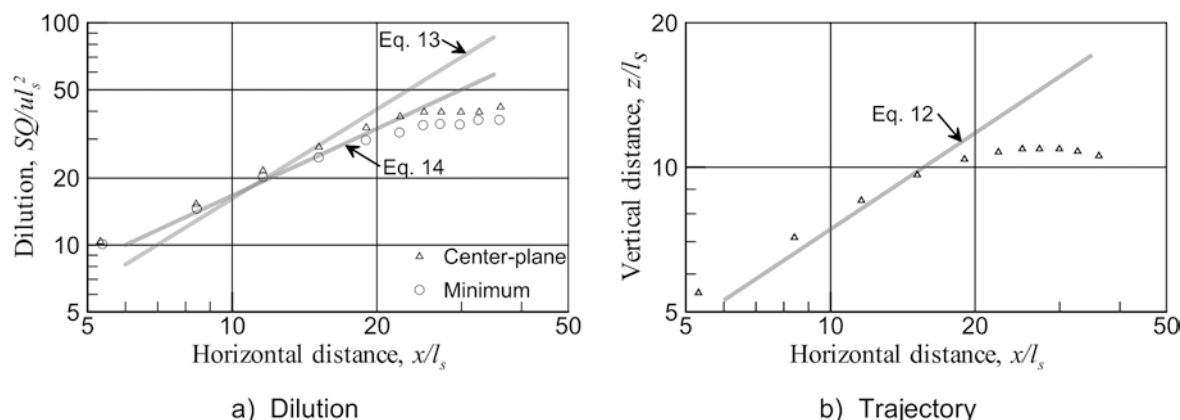


Fig. 12. Dilution and trajectory of vertical buoyant jet in a stratified cross flow

Vastly more data can be obtained with the 3DLIF system (and more easily) than with other techniques. For example, new data on minimum dilution and its 3D trajectory were obtained. These would be very difficult to obtain either from traditional point-based or PLIF measurement techniques. The minimum and center-plane dilutions were found to be initially very close, and then to gradually diverge, contradicting previous assumptions that their ratio is constant. The trajectory of the minimum dilution shows a much flatter trajectory than that of the center-plane dilution.

References

- Brücker C (1995) Digital-Particle-Image-Velocimetry (DPIV) in a scanning light-sheet: 3D starting flow around a short cylinder. *Exp Fluids* 19:255–263
- Brücker C (1997) Study of the three-dimensional flow in a T-junction using a dual scanning method for three-dimensional scanning (3-D SPIV). *Exp Therm Fluid Sci* 14:35–44
- Chu VH (1979) L. N. Fan's data on buoyant jets in crossflow. *J Hydraul Div-ASCE* 105(HY5):612–617
- Dahm WJA, Southerland K, Band Buch KA (1991) Direct, high resolution, four-dimensional measurements of the fine scale structure of $Sc \gg 1$ molecular mixing in turbulent flows. *Phys Fluids A* 3(5):1115–1127
- Dahm WJA, Su LK, Southerland KB (1992) A scalar imaging velocimetry technique for fully resolved four-dimensional vector velocity field measurements in turbulent flows. *Phys Fluids A* 4(10):2191–2206
- Daviero G (1998) Hydrodynamics of ocean outfall discharges in unstratified and stratified flows. PhD Thesis, School of Civil Engineering, Georgia Institute of Technology, Atlanta, GA
- Daviero GJ, Roberts PJW, Maile K (2001) Refractive index matching in large-scale stratified experiments. *Exp Fluids* 31:119–126
- Delo C, Smits AJ (1997) Volumetric visualization of coherent structure in a low Reynolds number turbulent boundary layer. Technical Report of the Department of Mechanical and Aerospace Engineering, Princeton University, NJ
- Deusch S (1998) Imaging of turbulent mixing by laser induced fluorescence and its application to velocity and velocity gradient measurements by a multi-patch 3D image correlation approach. PhD Thesis, Swiss Federal Institute of Technology
- Dimotakis PE, Miake-Lye RC, Papantoniou DA (1983) Structure and dynamics of round turbulent jets. *Phys Fluids* 26(11):3185–3192
- Ferrier A, Funk D, Roberts PJW (1993) Application of optical techniques to the study of plumes in stratified fluids. *Dynam Atmos Oceans* 20:155–183
- Fischer HB, List EJ, Koh RCY, Imberger J, Brooks NH (1979) Mixing in inland and coastal waters. Academic, New York
- Goldstein JE, Smits AJ (1994) Flow visualization of the three-dimensional, time-evolving structure of a turbulent boundary layer. *Phys Fluids* 6(2):577–586
- Guezennec YG, Zhao Y, Gieseke TJ (1994) High-speed 3-D scanning particle image velocimetry (3-D SPIV) techniques. Developments in laser techniques and applications to fluid mechanics, 7th International Symposium, pp 393–407
- Island TC, Patrie BJ, Mungal MG, Hanson RK (1996) Instantaneous three-dimensional flow visualization of a supersonic mixing layer. *Exp Fluids* 20:249–256
- Koochesfahani MM, Dimotakis PE (1985) Laser-induced fluorescence measurements of mixed fluid concentration in a liquid plane shear layer. *AIAA Journal* 23(11):1700–1707
- Kychakoff G, Paul PH, van Cruyningen I, Hanson RK (1987) Movies and 3-D images of flowfields using planar laser-induced fluorescence. *Appl Opt* 26(13):2498–2501
- Maas HG, Stefanidis A, Gruen A (1994) From pixels to voxels: tracking volume elements in sequences of 3-D digital images. ISPRS Commission III Symposium, Spatial Information from Digital Photogrammetry and Computer Vision, Munich, Sept 5–9, pp 539–546
- Merkel GJ, Dracos T, Rys P, Rys FS (1994) Turbulent mixing investigated by laser induced fluorescence. 5th European Turbulence Conference, Sienna, Italy
- Merkel GJ, Rys P, Rys FS, Dracos T (1996) Concentration and velocity field measurements in turbulent flows using laser-induced fluorescence tomography. *Appl Sci Res* 56:181–190
- Owen FK (1976) Simultaneous laser measurements of instantaneous velocity and concentration in turbulent mixing flows. AGARD-CP193, Paper 27
- Papanicolaou PN, List EJ (1988) Investigations of round vertical turbulent buoyant jets. *J Fluid Mech* 195:341–391
- Patrie BJ, Seitzman JM, Hanson RK (1994) Instantaneous three-dimensional flow visualization by rapid acquisition of multiple planar flow images. *Optical Engineering* 33(3):975–80
- Prasad RR, Sreenivasan KR (1990) Quantitative three-dimensional imaging and the structure of passive scalar fields in fully turbulent flows. *J Fluid Mech* 216:1–34
- Roberts PJW (1979) Line plume and ocean outfall dispersion. *J Hydraulics Division, ASCE* 105(HY4):313–330
- Roberts PJW, Snyder WH (1993) Hydraulic model study for the Boston Outfall. *J Hydraul Eng-ASCE* 119(9):970–1002
- Roberts PJW, Tian X (2002a) Application of three-dimensional laser-induced fluorescence to stratified turbulent mixing processes. Hydraulic Measurements and Experimental Methods Conf 2002, Estes Park, Colorado, July 28–August 1, 2002
- Roberts PJW, Tian X (2002b) New experimental techniques for validation of marine discharge models. *J Marine Syst*, in press
- Roberts PJW, Tian X (2003) Physical modeling of the Goro Nickel Outfall. School of Civil and Environmental Engineering, Georgia Institute of Technology, Atlanta, GA, June 3, 2003, p 60
- Roberts PJW, Snyder WH, Baumgartner DJ (1989) Ocean outfalls. *J Hydraul Eng-ASCE* 115(1):1–70

- Roberts PJW, Maile K, Daviero G (2001) Mixing in stratified jets. *J Hydraul Eng-ASCE* 127(3):194–200
- Roberts PJW, Hunt CD, Mickelson MJ (2002) Field and model studies of the Boston Outfall. 2nd Int Conf On Marine Waste Water Discharges MWWDD 2002, Istanbul, Sept16–20, 2002
- Rockwell D, Magness C, Towfighi J, Akin O, Corcoran T (1993) High image-density particle image velocimetry using laser scanning techniques. *Exp Fluids* 14:181–192
- Ruck B, Pavlovski B (2000) Laser tomography for flow structure analysis. *High Temp+* 38(1):106–117
- Tian X (2002) 3DLIF and its Applications to studies of the near field mixing of wastewater discharges. PhD Thesis, School of Civil and Environmental Engineering, Georgia Institute of Technology, Atlanta, GA
- Van Cruyningen I, Lozano A, Hanson RK (1990) Quantitative imaging of concentration by planar laser induced fluorescence. *Exp Fluids* 10:41–49
- Walker DA (1987) A fluorescence technique for measurement of concentration in mixing fluids. *J Phys E: Sci Instrum* 20: 217–224
- Webster DR, Roberts PJW, Raad L (2001) Simultaneous DPTV/PLIF measurements of a turbulent jet. *Exp Fluids* 30(1):65–72
- Winter M, Lam JK, Long MB (1987) Techniques for high-speed digital imaging of gas concentrations in turbulent flows. *Exp Fluids* 5:177–183
- Wright SJ (1977) Mean behavior of buoyant jets in a crossflow. *J Hydraul Div-ASCE* 103(HY5):499–513
- Wright SJ (1984) Buoyant jets in density-stratified crossflow. *J Hydraul Eng-ASCE* 110(5):643–656
- Yip B, Schmitt RL, Long MB (1988) Instantaneous three-dimensional concentration measurements in turbulent jets and flames. *Opt Lett* 13(2):96–98